In situ evidence for chirality-dependent growth rates of individual carbon nanotubes

Rahul Rao[1]*†, David Liptak[1,2], Tonya Cherukuri[1], Boris I. Yakobson[3] and Benji Maruyama[1]*

Chiral-selective growth of single-walled carbon nanotubes (SWNTs) remains a great challenge that hinders their use in applications such as electronics and medicine. Recent experimental[1,2] and theoretical[3,4] reports have begun to address this problem by suggesting that selectivity may be achieved during nucleation by changing the catalyst composition or structure. Nevertheless, to establish a rational basis for chiral-selective synthesis, the underlying mechanisms governing nucleation, growth, and termination of SWNTs must be better understood. To this end, we report the first measurements of growth rates of individual SWNTs through *in situ* Raman spectroscopy and correlate them with their chiral angles. Our results show that the growth rates are directly proportional to the chiral angles, in agreement with recent theoretical predictions[5,6]. Importantly, the evidence singles out the growth stage as responsible for the chiral distribution—distinct from nucleation and termination which might also affect the final product distribution. Our results suggest a route to chiral-selective synthesis of SWNTs through rational synthetic design strategies based on kinetic control.

The structure of a SWNT is equivalent to a graphene sheet rolled up into a cylinder; its structure is indexed by two integers (n, m), which depend on the diameter (d_t) and the angle of roll-up, also called the chiral angle $(\chi$; ref. 7). The electronic band structures of the SWNTs vary between semiconducting and metallic depending on the angle in which the graphene sheet is rolled. The chiral angle is therefore very important for charge transport, and precise control over the chirality during nanotube growth is critical for their large-scale use in electronic applications. However, the combination of an insufficient understanding of growth mechanisms, as well as a vast parameter space for SWNT growth inhibit progress in chiral-selective growth.

Previous post-growth measurements using spectroscopy[8,9] and transmission electron microscopy (TEM; ref. 10) to characterize chiral angle distributions have established a greater abundance of large chiral angle SWNTs in samples prepared by a range of synthesis methods, including chemical vapour deposition (CVD). However, it is unclear whether this abundance arises from a nucleation density or growth rate dependence on chirality. The resolution of this issue thus requires an *in situ* study of growth rate versus chiral angle. TEM has been used to image the nucleation and growth of carbon nanotubes *in situ*, although these experiments are challenging and suffer from low throughput[11–13]. So far, *in situ* TEM studies have not established a correlation between the growth rate and chiral angle. In contrast, *in situ* growth studies using optical absorption[14] and Raman spectroscopy[15–17] are able to provide quantitative growth kinetics data. However, these studies focus on the collective growth of many SWNTs, and cannot differentiate between nucleation density or growth rate as the cause of the abundance of large chiral angle SWNTs in CVD samples.

In this Letter, we address chiral-selectivity during SWNT growth by measuring the growth rates of individual SWNTs for the first time using *in situ* Raman spectroscopy and comparing their growth rates to their chiral angles. Our unique technique employs laser-induced heating of catalysts on silicon pillars, which are formed by etching Si/SiO₂ wafers (see Fig. 1a and Methods for more details). The small thermal mass of the pillars ($10 \times 10\,\mu m$), combined with thermal isolation from the wafer due to the oxide barrier, enables rapid heating to nanotube growth temperatures ranging from 835 °C to 990 °C. The scattered light from the pillar is used to collect Raman spectra, which are acquired continuously during the growth of a single SWNT within the laser spot. An example of a time series of Raman spectra collected during a growth experiment is shown as a waterfall plot in Fig. 1b, where initiation of SWNT growth is indicated by the appearance and subsequent increase in intensity of the G band at ~1,560 cm⁻¹. The G band is indicative of graphitic carbon and appears as a result of vibrations of carbon atoms in the tangential direction with respect to the nanotube axis[7]. (The position of the G band is downshifted relative to the room temperature position at ~1,590 cm⁻¹ because of the high temperature, consistent with previous temperature-dependent Raman studies on SWNTs)[18]. An extra peak at ~1,300 cm⁻¹, called the D band, appears as a result of disorder in the nanotube structure. Owing to the variation in growth temperatures of the individual SWNTs (835–990 °C), the G band intensities are normalized by the Bose thermal occupation factor $[1 - \exp(-\hbar\omega/k_B T)]^{-1}$ (ω is the G band frequency, T is the growth temperature, $\hbar$ is the reduced Planck constant and k_B is Boltzmann's constant) to account for the temperature dependence of the phonon populations. In addition, the G band intensities are normalized by the intensities of the Stokes Raman peaks from the silicon pillars to compare the *in situ* Raman data between different experiments.

The integrated intensities of the G bands are computed from the normalized *in situ* Raman spectra and plotted with respect to time to obtain a growth curve, as shown in Fig. 1c (see Supplementary Fig. S1 for more growth curves from individual SWNTs, as well as Supplementary Fig. S2 for an example of a pillar where no SWNT growth is observed at the end of the experiment). The growth curves are well-fit by a self-exhausting exponential equation of the form $G(t) = \nu\tau[1 - \exp(-t/\tau)]$, where $G(t)$, ν and τ are the area under the G band, the initial growth rate (related to the mass accretion rate) and the time constant for the reaction, respectively[15,16,19]. This exponential growth equation is typically applied to the collective growth and termination of SWNT ensembles[16,19], where individual SWNTs may nucleate and terminate at different times and the reaction time constant is an ensemble contribution from many SWNTs. Interestingly, in our experiments the *in situ* growth curves
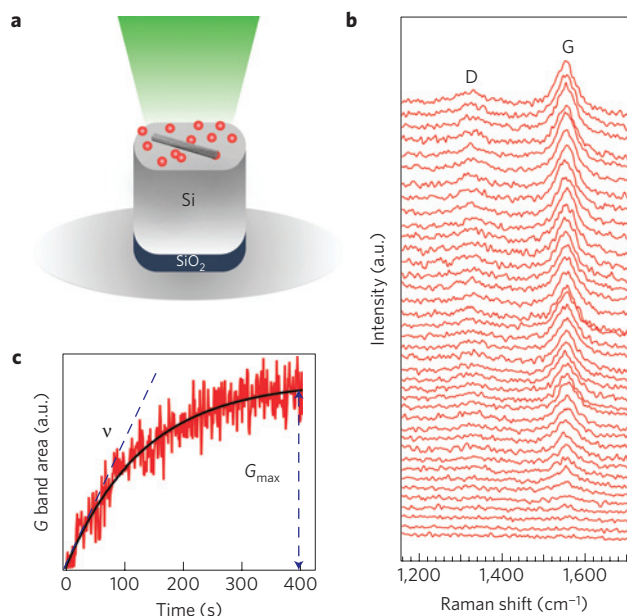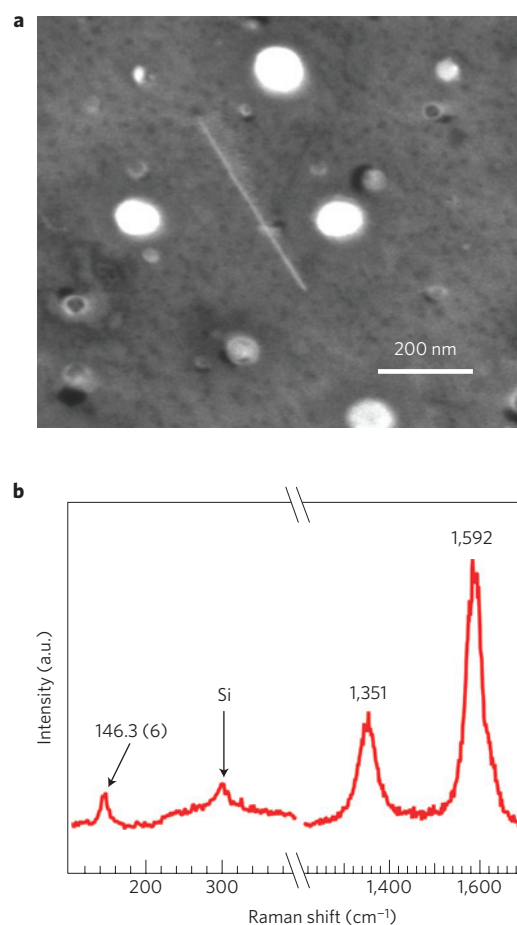
Figure 1 | *In situ* Raman spectroscopy and growth of a SWNT. a, Schematic showing laser-induced growth of an individual SWNT from a catalyst nanoparticle on a thermally isolated silicon pillar. **b**, Waterfall plot showing the temporal evolution of the disorder-induced D band and the graphitic G band from a growing SWNT. The spectra are plotted with increasing time from bottom to top and are offset for clarity. **c**, Growth curve obtained by plotting the calculated G band area versus time from the normalized *in situ* Raman spectra, fit to an exponential form. The dashed lines in **c** indicate the initial growth rate, ν, and the final G band intensity, G_{max}.

Figure 2 | SEM image and Raman spectrum from an individual SWNT. a,b, Scanning electron microscope image of an individual SWNT (**a**) and the corresponding room temperature Raman spectrum (**b**) from the same SWNT exhibiting a single peak in the low-frequency RBM region and narrow D and G bands in the high-frequency region. The deconvoluted linewidth (full-width at half-maximum) of the RBM is indicated in parentheses. The peaks appearing between 200 and 400 cm⁻¹ in **b** are due to the silicon substrate.

obtained from individual SWNTs are also observed to follow exponential growth and decay kinetics. Although the termination mechanism for individual SWNTs may be due to a time-dependent catalyst mass loss phenomenon[20], this is an area of active study beyond the scope of this Letter.

Post-growth scanning electron microscopy (SEM) and Raman analysis confirm that the *in situ* Raman spectra presented in Fig. 1b are from an individual SWNT. As shown in the SEM image in Fig. 2a, only one SWNT is observed within the area from which the *in situ* Raman spectra are acquired. It should be noted that other forms of carbon are also observed on the pillars. However, owing to non-resonant conditions they do not contribute significantly to the *in situ* Raman spectra. Further evidence for the presence of a single SWNT is provided by a post-growth (room temperature) Raman spectrum from the same SWNT which exhibits narrow linewidths, and the appearance of only one peak in the low-frequency radial breathing mode (RBM) region, as shown in Fig. 2b (further SEM images, a post-growth Raman spectrum and a Raman intensity map of a G band from an individual SWNT are shown in Supplementary Fig. S3; refs 21,22). From the SEM images and RBM frequencies collected from various individual SWNTs (Supplementary Fig. S4 for post-growth Raman spectra from various individual SWNTs), we determine their lengths and diameters, respectively. We find, as expected, that the lengths measured by SEM are directly correlated to the maximum G band intensities (G_{max} in Fig. 1c) divided by the nanotube diameters (Supplementary Fig. S4). This correlation is then used to convert our *in situ* measured initial growth rates (ν) to linear growth rates.

The chiral indices (n, m) for the SWNTs are assigned by comparing the RBM peak frequencies with the well-known 'Kataura plot', which maps transition energies in the electronic density of states (Van Hove singularities) of the SWNTs to the tube diameters[23] (see Supplementary Figs S5–S7 and detailed discussion

on the chiral index assignment for each SWNT). We make chiral index assignments for nine SWNTs, from which we obtain chiral angles ranging from 11.3° to 28.7°. Further confirmation for our chiral index assignments is obtained by calculating the diameters of the SWNTs according to the formula $d_t = 0.78(n^2 + nm + m^2)^{1/2}$ Å. The calculated diameters relate very well to the experimentally observed RBM frequencies using the relation $\omega_{RBM} = 227/d_t(1 + 0.0578 \times d_t^2)^{1/2}$ (Supplementary Fig. S6), which is an established general relationship between diameter and RBM frequency for SWNTs (ref. 24).

Figure 3a shows the plot of the linear growth rates for the nine SWNTs against their chiral angles. The positive correlation between the linear growth rate and χ is clearly evident. Also plotted in Fig. 3a is a theoretical calculation (red line and data points) based on the dislocation mechanism of SWNT growth[5], which shows good agreement with the experimental data. We note here that although chiral index assignments using RBMs are not completely unambiguous, we also consider alternate chiral index assignments based on an analysis of resonance windows and RBM frequencies, and find that the positive correlation between growth rates and chiral angles shown in Fig. 3a remains persuasive (see Supplementary Fig. S8 and related discussion on alternate chiral index assignments for the SWNTs). Furthermore, although the
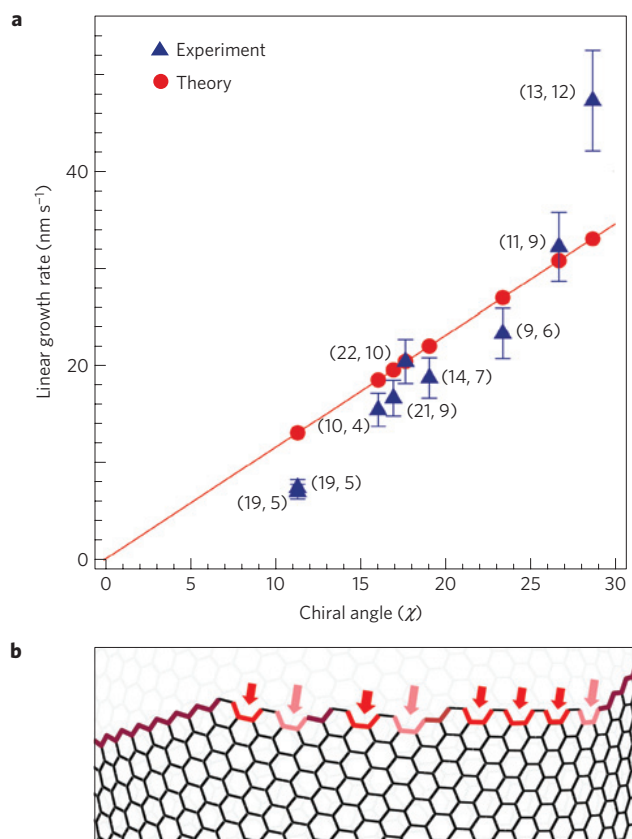
Figure 3 | Chirality-dependent growth of SWNTs. a, The linear growth rates (blue triangles) along with assigned (n, m) chiral indices are plotted against the chiral angle χ. The data clearly demonstrate a correlation between the growth rate and χ. The vertical error bars correspond to a $\pm 10\%$ error in estimating the growth rates. The red line represents the growth rate calculated from the dislocation mechanism of SWNT growth[5] along with values (red circles) predicted from the model for the experimentally observed SWNTs (see main text for further discussion). **b**, A schematic of the structure of a SWNT edge. The arrows indicate sites that are highly active (kinks, light red), moderately active (armchair, red) and inactive (zigzag, dark red) for carbon addition.

growth temperatures are different for each experiment, we do not find a significant effect of temperature on the growth rates or chiral angles of the SWNTs (see Supplementary Fig. S9 and text for discussion of the temperature dependence).

The relation of linear growth rate with the chiral angle, as seen in Fig. 3a, is derived naturally within the dislocation theory of SWNT growth[5], according to which the chirality of the SWNT is crystallographically equivalent to a screw dislocation along the axis with a variety of edge sites for carbon addition, as shown in the schematic in Fig. 3b. Consequently, the number of kinks (equal to the chiral index m) at the growing edge of the nanotube serve as active docking sites for newly arriving carbon dimers (C_2), resulting in a mass growth rate $\sim m$, and a linear growth rate (speed of length increase) that is proportional to $m/d_t \sim \sin(\chi)$. Indeed, adding C_2 to a kink (light red in Fig. 3b) simply shifts its location by one lattice parameter, with no change in the kind of dangling bonds and therefore no energy penalty. In contrast, adding C_2 or C_3 to a zigzag terrace (red in Fig. 3b) creates a configuration of prohibitive energy, $E_Z > k_B T$ ($E_Z \sim 1-2$ eV; ref. 5), according to density functional theory calculations. On the other hand, adding carbon to an armchair terrace (dark red in Fig. 3b) slightly changes the number of dangling bonds (replacing the two of armchair-type by two of zigzag-type), and so a small energy cost

is incurred, E_A (~ 0.1 eV), according to density functional theory calculations[25]. Neglecting this small obstacle, that is assuming that the armchair terrace is just as good for carbon accretion as the kink-sites, one arrives at a simple relationship for the linear growth rate, $K \sim \sin(\chi)$, which is also plotted in Fig. 3a (red line and data points)[5]. A more general dependence on the chiral angle can be readily obtained through geometry analysis[25] and by counting the number of different docking sites, resulting in a family of curves between K and χ (see Supplementary Fig. S10 and related discussion). We find, however, that a refinement of these details (non-zero activity of the zigzag sites or reduced activity of the armchair sites, relative to the kinks) is not called for: it does not bring the theoretical dependence of $K(\chi)$ closer to the experimental data, which thus favour the simplest choice above. It is important to emphasize here that we are able to correlate the theoretical prediction with the observed growth rates directly. In contrast, previous comparisons have been made possible only with the overall chiral distribution abundance of the final product, leaving obscure its origin from either nucleation, or growth rates, or other factors.

Finally, we realize that our experiments are conducted in a unique set-up and that the conditions for laser-induced cold-wall CVD are different from more typical thermal CVD processes. Nevertheless, the good agreement between our experimental and theoretical results at the individual nanotube level with post-growth chirality distribution studies of SWNTs grown from a variety of processes[8,9] is a strong indication that, in general, the SWNT growth rate is directly proportional to its chiral angle. By using our unique technique to measure and correlate growth rates to the chiral angle we have firmly established the viability of the dislocation mechanism of SWNT growth. Although these results do not preclude the possibility of chirality control at the nucleation stage[1,2,25], our work provides a rational basis for the design of new catalyst systems that determine the yield of chiral-selected nanotubes by kinetic control.

Methods

***In situ* growth experiments.** SWNT growth takes place by means of laser-induced CVD within a high-vacuum chamber coupled to a Raman microscope. The samples consist of $10 \times 10\,\mu$m pillars of silicon, spaced $40\,\mu$m apart, which are formed by deep reactive ion etching of the $10\,\mu$m top layer of a Si/SiO$_2$ substrate. The small thermal mass of the pillar allows for efficient heating to the growth temperature (from 835 to 990 °C) using a few 100 mW of laser power. The oxide barrier layer below the pillars enhances heating by restricting conductive heat transfer between the pillar and the underlying bulk silicon substrate. Thin sputtered films (2 nm) of iron are used as catalysts for nanotube growth. Before each growth experiment, the chamber is pumped down to a base pressure of $\sim 9 \times 10^{-6}$ torr, then backfilled with flowing argon to the growth pressure of 25 torr. The gas environment within the chamber is monitored continuously with a residual gas analyser to make sure that the water vapour or oxygen levels remain low (partial pressures $<5 \times 10^{-7}$ torr). Next, argon (research grade, 99.99997% pure) and hydrogen gas (research grade, 99.9999 % pure) flows are initiated at 25 and 10 s.c.c.m., respectively. The Raman excitation laser (532 nm) is focused on each pillar through a long working distance ×40 objective lens (the laser spot size is $\sim 7\,\mu$m) and controlled heating is achieved by manipulating the laser power. The power densities on the pillars range from 3×10^5 to 6×10^5 W cm^{-2}. The silicon pillar temperature is estimated from the ratio of the anti-Stokes to Stokes peaks using the following relation:

$$\frac{I_{AS}}{I_S} = \frac{(\nu_0 + \nu_1)^4}{(\nu_0 - \nu_1)^4} \exp\left(-\frac{hc\nu_1}{k_B T}\right)$$

where I_{AS} and I_S are the anti-Stokes and Stokes intensities respectively, h is the Planck constant, c is the speed of light, and ν_0 and ν_1 are the laser line and silicon peak frequencies, respectively. Using the above equation, temperatures for our growth measurements are computed with an accuracy of ± 25 °C.

Once the substrate pillar reaches the target growth temperature (typically within 1–5 min), 5 s.c.c.m. of ethylene (research grade, 99.995% pure) is introduced into the chamber to initiate nanotube growth. Raman spectra between $-2,000$ and $3,000$ cm^{-1} are collected and saved at 1 s intervals during the growth experiment. Nanotube nucleation and growth is detected by the appearance, and increase in intensity of a peak around the G band region between 1,500 and 1,600 cm^{-1}. The ethylene flow is turned off after the G band intensity stops increasing further, thus indicating termination of growth.

Post-growth analysis. Following growth, the areas under the G bands are calculated for each normalized spectrum and plotted against time to obtain growth curves for the SWNTs, which are then fitted to exponential equations (see main text for details) that generate the initial growth rates and time constants for the individual SWNTs. In addition, *ex situ* Raman spectra are collected using a Renishaw inVia Raman microscope with 532, 633, and 514.5 nm laser excitations to characterize RBMs. The SWNT lengths are estimated from high-resolution scanning electron microscopy images obtained using Hitachi 5200 and FEI Sirion electron microscopes operating at 3 and 5 kV acceleration voltages, respectively.

References

1. Chiang, W-H. & Sankaran, R. M. Linking catalyst composition to chirality distributions of as-grown single-walled carbon nanotubes by tuning Ni_xFe_{1-x} nanoparticles. *Nature Mater.* **8,** 882–886 (2009).
2. Harutyunyan, A. R. *et al.* Preferential growth of single-walled carbon nanotubes with metallic conductivity. *Science* **326,** 116–120 (2009).
3. Reich, S., Li, L. & Robertson, J. Control the chirality of carbon nanotubes by epitaxial growth. *Chem. Phys. Lett.* **421,** 469–472 (2006).
4. Koziol, K. K. K., Ducati, C. & Windle, A. H. Carbon nanotubes with catalyst controlled chiral angle. *Chem. Mater.* **22,** 4904–4911 (2010).
5. Ding, F., Harutyunyan, A. & Yakobson, B. Dislocation theory of chirality-controlled nanotube growth. *Proc. Natl Acad. Sci. USA* **106,** 2506–2509 (2009).
6. Dumlich, H. & Reich, S. Chirality-dependent growth rate of carbon nanotubes: A theoretical study. *Phys. Rev. B* **82,** 085421 (2010).
7. Saito, R., Dresselhaus, G. & Dresselhaus, M. S. *Physical Properties of Carbon Nanotubes* (Imperial College Press, 1998).
8. Bachilo, S. M. *et al.* Narrow (n, m)-distribution of single-walled carbon nanotubes grown using a solid supported catalyst. *J. Am. Chem. Soc.* **125,** 11186–11187 (2003).
9. Miyauchi, Y., Chiashi, S., Murakami, Y., Hayashida, Y. & Maruyama, S. Fluorescence spectroscopy of single-walled carbon nanotubes synthesized from alcohol. *Chem. Phys. Lett.* **387,** 198–203 (2004).
10. Sato, Y. *et al.* Chiral-angle distribution for separated single-walled carbon nanotubes. *Nano Lett.* **8,** 3151–3154 (2008).
11. Hofmann, S. *et al. In situ* observations of catalyst dynamics during surface-bound carbon nanotube nucleation. *Nano Lett.* **7,** 602–608 (2007).
12. Yoshida, H., Takeda, S., Uchiyama, T., Kohno, H. & Homma, Y. Atomic-scale *in situ* observation of carbon nanotube growth from solid state iron carbide nanoparticles. *Nano Lett.* **8,** 2082–2086 (2008).
13. Sharma, R., Rez, P., Treacy, M. M. J. & Stuart, S. J. *In situ* observation of the growth mechanisms of carbon nanotubes under diverse reaction conditions. *J. Electron Microsc.* **54,** 231–237 (2005).
14. Puretzky, A. A., Geohegan, D. B., Jesse, S., Ivanov, I. N. & Eres, G. *In situ* measurements and modeling of carbon nanotube array growth kinetics during chemical vapor deposition. *Appl. Phys. A* **81,** 223–240 (2005).
15. Chiashi, S., Murakami, Y., Miyauchi, Y. & Maruyama, S. Cold wall CVD generation of single-walled carbon nanotubes and *in situ* Raman scattering measurements of the growth stage. *Chem. Phys. Lett.* **386,** 89–94 (2004).
16. Picher, M., Anglaret, E., Arenal, R. & Jourdain, V. Self-deactivation of single-walled carbon nanotube growth studied by *in situ* Raman measurements. *Nano Lett.* **9,** 542–547 (2009).
17. Li-Pook-Than, A., Lefebvre, J. & Finnie, P. Phases of carbon nanotube growth and population evolution from *in situ* Raman spectroscopy during chemical vapor deposition. *J. Phys. Chem. C* **114,** 11018–11025 (2010).
18. Raravikar, N. *et al.* Temperature dependence of radial breathing mode Raman frequency of single-walled carbon nanotubes. *Phys. Rev. B* **66,** 235424 (2002).
19. Einarsson, E., Murakami, Y., Kadowaki, M. & Maruyama, S. Growth dynamics of vertically aligned single-walled carbon nanotubes from *in situ* measurements. *Carbon* **46,** 923–930 (2008).
20. Amama, P. B. *et al.* Role of water in super growth of single-walled carbon nanotube carpets. *Nano Lett.* **9,** 44–49 (2008).
21. Rao, R., Menendez, J., Poweleit, C. D. & Rao, A. M. Anharmonic phonon lifetimes in carbon nanotubes: Evidence for a one-dimensional phonon decay bottleneck. *Phys. Rev. Lett.* **99,** 047403–047404 (2007).
22. Jorio, A. *et al.* Linewidth of the Raman features of individual single-wall carbon nanotubes. *Phys. Rev. B* **66,** 115411 (2002).
23. Jorio, A. *et al.* Structural (n, m) determination of isolated single-wall carbon nanotubes by resonant Raman scattering. *Phys. Rev. Lett.* **86,** 1118–1121 (2001).
24. Araujo, P. T. *et al.* Nature of the constant factor in the relation between radial breathing mode frequency and tube diameter for single-wall carbon nanotubes. *Phys. Rev. B* **77,** 241403 (2008).
25. Liu, Y., Dobrinsky, A. & Yakobson, B. I. Graphene edge from armchair to zigzag: The origins of nanotube chirality? *Phys. Rev. Lett.* **105,** 235502 (2010).

Author contributions

R.R. designed and conducted the experiments. D.L., R.R. and T.C. designed and constructed the instrumentation. D.L. wrote the software for data acquisition and analysis. B.I.Y. provided the theoretical analysis. B.M. guided the research direction and assisted in data analysis. All authors contributed to the writing and editing of the manuscript.